Optimization of the Charge Motion in Sewage Gas-Driven Internal Combustion Engines for Combined Heat and Power Units

Lucas Konstantinoff, Christoph Pfeifer, Martin Pillei, Uwe Trattnig, Thomas Dornauer, Lukas Möltner

***Abstract*—** In this study, a goal-oriented optimization of the charge motion in a sewage gas-driven internal combustion engine of a combined heat and power unit was investigated to increase efficiency. The swirl flow influenced by the geometry next to the valve seats was considered in particular. For this purpose, experiments took place on a flow bench to integratively quantify the swirl flow; laser-optical methods were also applied to determine flow patterns in discrete plains inside the cylinder. In detail, we compared two cylinder heads that differ in their geometry in the immediate vicinity to the inlet valve seats. Following the investigations of in-cylinder flow characteristics, combustion analysis on a test engine was conducted via a cylinder pressure indication system for partial and full-load operation points. The framework of the optimization measures consists of the mandatory NO_x limit of 500 $mg \cdot m^{-3}$ and a limit in the maximum working pressure that could be met. A summary of the results reveals that the new valve seat design has a significant enhancing impact on the swirl motion and, hence, upon the combustion. A comparative consideration between the two cylinder heads shows that the increased swirl motion results in faster combustion and, therefore, higher efficiency. Summing up, the geometrical modifications close to the valve seat result in increased turbulence intensity, and it was proven that this intensification raises the ratio of efficiency by 1.6%.

***Keywords*—** Combined heat and power, sewage gas, turbulent combustion, charge motion

This research project was funded as a cooperative and innovative project by the Tyrolean government (WIF-540-02-00200/01-0010). The authors gratefully acknowledge all support that the Tyrolean government and the cooperating research partners, PGES, ECI-M, and MCI, provided.

Lucas Konstantinoff is with the Department of Technology and Life Sciences, Management Center Innsbruck - Austria (e-mail: lucas.konstantinoff@mci.edu).

Christoph Pfeifer is with the Institute for Chemical and Energy Engineering, University of Natural Resources and Life Sciences Vienna - Austria (e-mail: christoph.pfeifer@boku.ac.at).

Martin Pillei is with the Department of Technology and Life Sciences, Management Center Innsbruck - Austria (e-mail: martin.pillei@mci.edu).

Uwe Trattnig is with the Institute Energy, Transport and Environmental Management, FH Joanneum - Austria (e-mail: uwe.trattnig@fh-joanneum.at).

Thomas Dornauer is with the Department of Technology and Life Sciences, Management Center Innsbruck - Austria (thomas.dornauer@mci.edu).

Lukas Möltner is with the Department of Technology and Life Sciences, Management Center Innsbruck - Austria (phone: + 43 512 2070 – 4132; e-mail: lukas.moeltner@mci.edu).

I. INTRODUCTION

This paper is based on the pre-published study "Turbulent Combustion in Piston Engines driven by Sewage Gas for the Cogeneration of Heat and Power" in [1] and represents an extended version of the findings of this research project.

Reciprocating piston engines are one of the most effective and reliable options to convert burnable gases to electric power and heat energy. Sewage gas and other methane-containing gases (e.g., biogas) have gained importance due to better knocking resistance, favorable combustion characteristics and lower overall CO_2 emissions in comparison to conventional fuels, such as natural gas. The demand for efficient internal combustion engines (ICEs) that are able to meet current and future global emission legislations motivates recent research and development activities [2].

The utilization of non-fossil gases with varying compositions and real-life operation conditions, including partial load operation, necessitates adaptations for ICEs to ensure the highest possible efficiency regarding CO_2 and NO_x emissions [3], [4].

A comparably simple but nevertheless effective method to improve an engine's efficiency is to optimize the in-cylinder flow characteristics, which are mainly influenced by the combustion-chamber design (e.g., cylinder head, valve seat, inlet port geometry and piston) [5], [6]. In combination with highly accurate adjustments of engine control parameters (e.g., firing point (FP), ignition duration (ID), boost pressure and air/fuel-ratio (λ)), high-turbulence intensities have the potential to significantly increase efficiency [7], [8].

Fundamental knowledge of the relation between component geometries and their flow characteristics and combustion performance, particularly during varying load scenarios, is substantial for the design and development of advanced engine components.

Hence, the goal of the present research was to investigate the implications of new valve-seat geometries on volumetric efficiency and on the internal combustion in a state-of-the-art sewage gas-driven ICE of a combined heat and power unit (CHP) [9].

II. State of the Art

A. Internal Combustion

In almost every internal combustion process, combustion velocity is strongly influenced by the surrounding turbulence patterns. The kinetic energy of turbulence, as well as the size and propagation of occurring eddies, have a significant influence on the progress of combustion and, hence, the combustion rate.

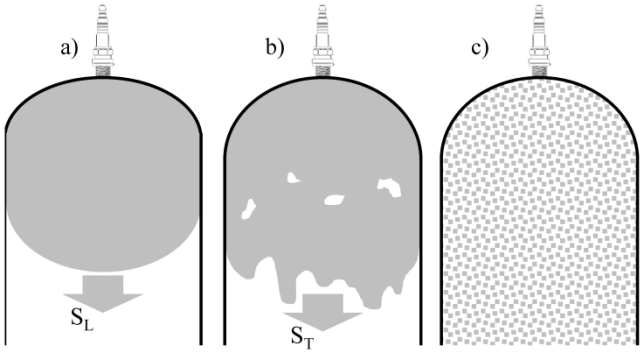

Fig. 1: Types of flame propagation with respect to the intensity of turbulence [1]

Fig. 1 illustrates three different combustion regimes of deflagration caused by various turbulence intensities [10]. A low turbulence intensity results in an enclosed propagation of a filmy flame front with laminar flame velocity v_l, depicted in Fig. 1 a). Increasing turbulence leads to a convolution of the flame front and the formation of single flamelets. The flame front partly disintegrates and moves with the turbulent velocity v_t, as shown in Fig. 1 b). If the turbulence's intensity is further increased, the flame front converts into a homogeneous admixture of already burnt and unburnt gases (= ideal stirred reactor) and presents the highest combustion rates. Subsuming the velocity of the flame propagation and, thus, the combustion rate are strongly influenced by the turbulence inside the combustion chamber [11], [12].

According to [13]–[15], the laminar flame speed S_L can be expressed by (1). S_L is a function of the density ρ and a specific reaction rate $\dot{\omega}$ [15].

$$S_L = \left(\frac{\alpha \cdot \dot{\omega}}{Ze \cdot \rho}\right)^{\frac{1}{2}} \quad (1)$$

The variable α is defined by the quotient of heat conductivity λ and the product of density ρ and heat capacity c_p.

$$\alpha = \frac{\lambda}{\rho \cdot c_p} \quad (2)$$

Ze stands for the Zeldovich Number, which can be calculated through (3). This number primarily depends on the flame temperature T_f, since it is usually far higher than the initial temperature of the reactants T_0.

$$Ze = \frac{E \cdot (T_f - T_0)}{\mathrm{R} \cdot T_f^2} \quad (3)$$

Following these considerations, lean burn engines would reveal a disadvantage compared to stoichiometric operating engines due to lower combustion temperatures. However, it is known that within certain limits, turbulent combustion leads to faster combustion [16]. This principle may be explained through (4) and (5) [17].

$$\frac{S_T}{S_L} = \frac{A_T}{A_L} \quad (4)$$

Damkoehler [17] sets the speed ratio of turbulent flame speed S_T and laminar flame speed S_L in relation to a ratio of turbulent- (A_T) and a laminar flame area A_L by assuming equal densities of the educts in these two cases. Further, he introduces a turbulent velocity fluctuation $U´$ that leaves (5).

$$S_T = S_L\left(1 + \frac{U´}{S_L}\right) \quad (5)$$

The enlarged flame surface in the case of increased turbulence is particularly illustrated in Fig. 1, case b). Considering (5), the higher flame speed in the case of enhanced turbulence becomes comprehensible. Knowing that $U´$ is approximately proportional to the rotational speed of the engine, it is possible to explain the change of the flame speed at partial-load operation [18], [19]. If turbulence is maintained in limits where no local flame extinctions occur, there is a good correlation between this model and experimental deflagration investigations [19].

In contrast to combustion processes caused by deflagration, the characteristics of detonations show multiply higher velocities of the flame front (> 1000 m·s^{-1}) and flame propagation promoted by a pressure wave maintained by chemical reactions and, thus, by the heat release of the combustion [20]–[22].

B. Thermodynamic Background

From a thermodynamic standpoint, internal combustion should occur infinitely fast so that all of the heat released is utilized to increase the temperature inside the combustion chamber. The more time needed for combustion, the more energy is consumed for volume work during the expansion stroke. Consequently, this fact results in a reduced maximum working temperature and, hence, a lower ratio of efficiency [23].

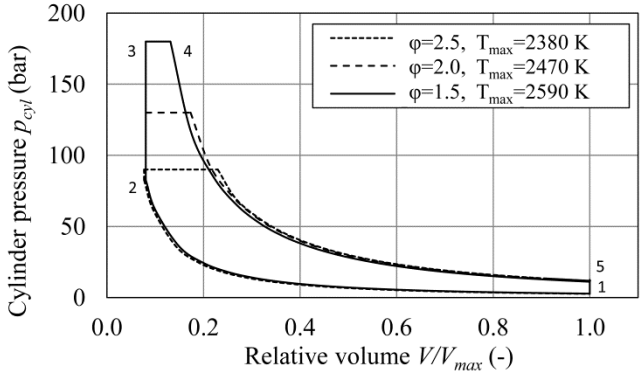

Fig. 2: Simplified Seiliger cycle for the test engine for volume ratios (*V4/V3*) of φ = 1.5, φ = 2.0, φ = 2.5 and maximum temperatures; compression ratio ε = 14, boost pressure p_{boost} = 1.54 bar, c_p = 1004 J·(kgK)$^{-1}$, c_v = 717 J·(kgK)$^{-1}$, $Q_{in\ total}$ = 8000 J

Fig. 2 explains the principle of the advantageous turbulent combustion concept strongly simplified by the Seiliger cycle modeled by using test engine specifications and real-life process parameters. After ignition (at state 2 in Fig. 2), the combustion occurs slowly when deflagration lasts far into the expansion stroke, reducing usable maximum working temperature and showing high volume ratios φ. If rapid combustion occurs, more of the heat input can be used to increase the working pressure and, hence, the usable working temperature, represented by lower-volume ratios.

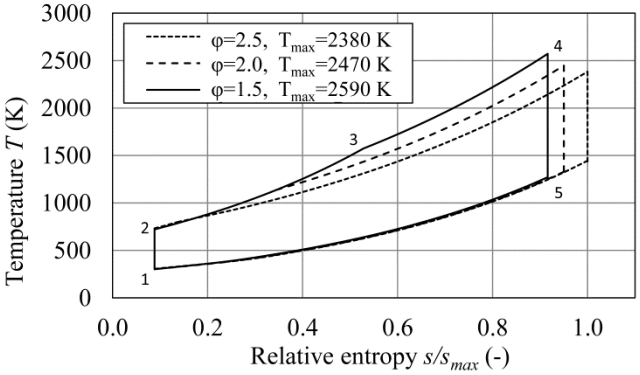

Fig. 3: Simplified T,s- diagram of the shown Seiliger cycle with normalized specific enthalpies and working temperatures resulting from volume ratios of φ = 1.5, φ = 2, φ = 2.5, as shown in Fig. 2

Fig. 3 shows the simplified Seiliger cycle in the T,s- diagram. As described above, a lower volume ratio φ results in higher working temperatures inside the combustion chamber. For improved comparability, the engine parameters used for these calculations were chosen in accordance with the test engine shown in Table 1 (III.A).

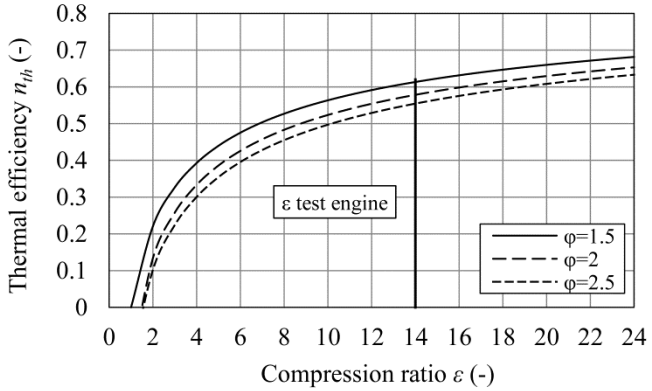

Fig. 4: Potential gain in efficiency with optimized burning velocities

Fig. 4 presents the implications of the considered volume ratios φ with respect to the compression ratio and thermal efficiency. A comparison between Fig. 2 and Fig. 4 illustrates that faster combustion, identified by a low volume ratio φ, increases the maximum working temperature and, thus, the thermal efficiency ratio [23]. Therefore, a target-oriented optimization of the charge motion inside the combustion chamber has the potential to increase the engine's efficiency.

C. Charge Motion

The charge motion in the combustion chamber is the strongest determinant for heat and mass transfer during internal combustion and heat dissipation via the cylinder wall, cylinder head and piston. The charge motion can be classified into three primary types: swirl, tumble and squish flows [18]. The flow patterns are illustrated in Fig. 5.

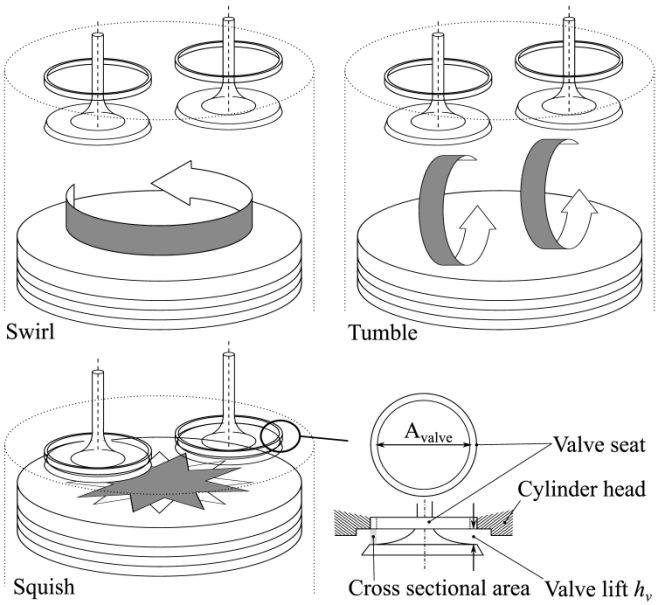

Fig. 5: Schematic illustration of swirl, tumble and squish flow patterns and valve seat construction and geometries

The first flow type, which is the swirl flow, is a radial rotating motion of inflowing gas that can be provoked either by a tangential geometry of the inlet channel or by the geometry next to the valve seat. It has been reported that geometric measures in the vicinity of the valve seat have the potential to increase swirl, particularly at small valve lifts [24].

Contrary to the swirl flow, the tumble describes a rotating charge motion in a vertical direction that can be induced by the inlet geometry and/or shape of the piston head. The effect of tumble is only available as long as the piston is not moving upwards, hence in early stages of compression.

Squish flows are the product of displacement effects between the combustion chamber and the upward-moving piston. Squish flows are only of importance close to top dead center (TDC) and result in a high heat release at an early stage of combustion [25].

As all types of charge motion increase turbulence of the load, the swirl flow is the most robust as it is not mitigated by the up-moving piston.

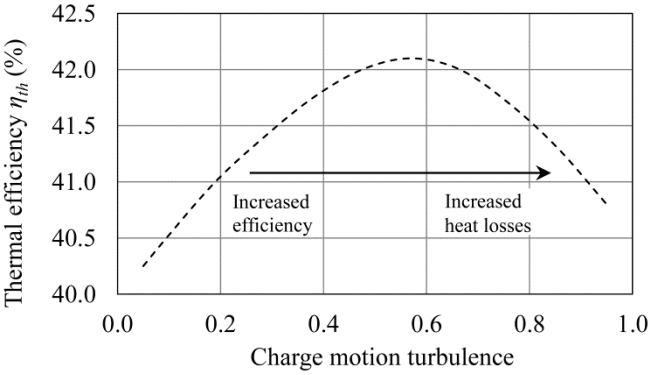

Fig. 6: Influence of charge motion on combustion efficiency and heat losses througout walls

Fig. 6 shows the effect of increasing charge motion on the efficiency of the combustion. There is a range in which increased swirl turbulence can have different effects on the outcome. As described earlier in this paper, higher turbulence is related to higher combustion speed and, hence, better combustion efficiency, resulting from a higher usable working temperature. This effect, however, is technically limited by increased heat losses throughout the wall that might overcompensate for assets caused by a faster combustion [24].

III. Methodology and Experimental Set Up

A. Test Engine and Cylinder Heads

A state-of-the-art biogas cogeneration unit with a nominal power output of 150 kW (P_{ISO}) was used for this research. The test engine was connected to the municipal heat and electricity grids, providing a real-life test-engine set-up. Table 1 shows relevant technical engine specifications.

Table 1: Technical specifications of the test engine

ISO standard power (mech.)	P_{ISO}	kW	150
Air/fuel ratio	λ	-	1.55
Compression ratio	ε	-	14:01
Brake mean effective pressure	BMEP	bar	15.8
Electrical efficiency	η_{el}	%	40.2
Mechanical efficiency	η_{mech}	%	42.2
Number of cylinders		-	4

The newly designed cylinder head (referred to as *HiGas*) features no differences in inlet manifold geometry compared to the baseline version. However, it deviates near the inlet valve seats, where sickle-shaped cuts have been made to change the flow pattern [26]–[28]. Fig. 7 is a comparative depiction of the baseline cylinder head and the newly developed model (right).

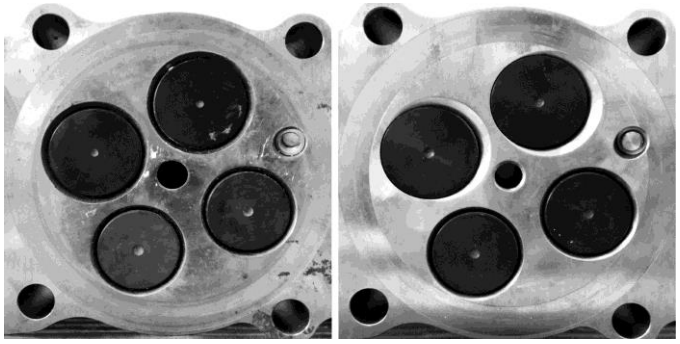

Fig. 7: Baseline (left) and new HiGas (right) cylinder head with sickle-shaped cuts near the inlet valves' seats

In the newly developed model, the sickle shape near the first inlet valve of the new cylinder head is directed toward the second inlet valve and spark plug, and the second sickle shape is targeted tangentially to the wall to enhance rotational gas movement. The baseline cylinder head is a state-of-the-art cylinder head that brings high efficiency and combustion performance as a standard cylinder head (Table 1). Nonetheless, a new design needed to be implemented as an approach to reach combustion performance converging real and theoretical efficiencies.

B. Experiments on the Static Flow Bench

To allow examination of the different cylinder head versions, a static flow bench was designed and constructed at *MCI* Innsbruck, Fig. 8. Within the flow bench a blower provides the necessary differential pressure to supply the air flow through the cylinder head at a set valve lift. The air flows through the cylinder head, which is mounted to a cylinder-head-specific interchangeable adapter and then to the swirl meter. The distance between the rectifier's top surface and the cylinder head's sealing surface h_z depends on the cylinder's bore diameter D_{bore} and is set to $h_z = D_{bore} \cdot 0.7$. The swirl meter is a low-friction mounted flow rectifier connected to a torque meter. The angular momentum of the intake air is transferred into a torque meter and can be quantified.

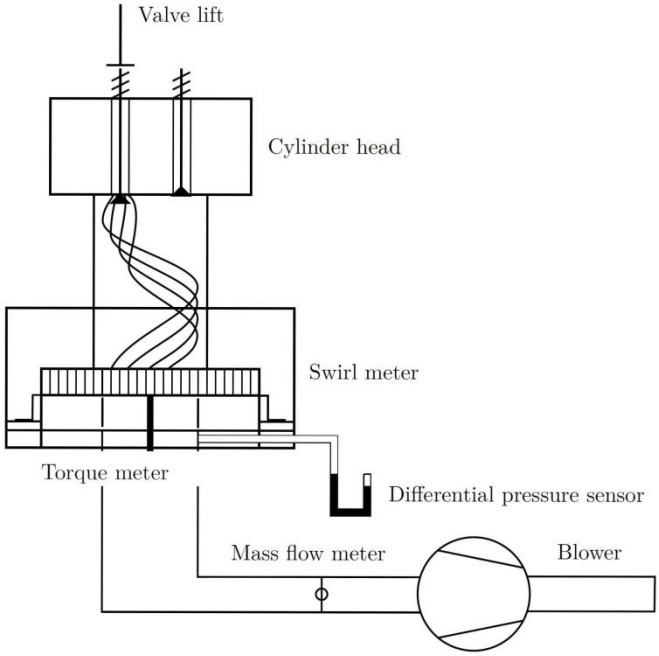

Fig. 8: Schematic set up of the constructed static flow bench

The air flow and its angular momentum, which is generated by the sickle-shaped cut and inlet port of the cylinder head, were measured at different valve lifts. In accordance with the integrative method described by *Tippelmann*, a torque meter was used to capture the complete rotational motion of the flow pattern [26].

Flow and swirl coefficients were calculated using the information received on flow and torque.

The measured torque M equals the initial angular momentum İ of the air flow by assuming a frictionless bearing of the flow rectifier and a fully rectified air flow. *Tippelmann* defines the torque as being proportional to the square of the volumetric flow rate V̇ and the density ρ of air (6).

$$M = \dot{I} = D^* \cdot \dot{V}^2 \cdot \rho \tag{6}$$

The factor D^* describes the relationship between the swirl number K_S and the cylinder diameter d_{cyl} (7).

$$D^* = \frac{2 \cdot K_S}{d_{cyl}} \tag{7}$$

Combining and rearranging (6) and (7) delivers the swirl coefficient with (8).

$$K_S = \frac{M \cdot \rho \cdot d_{cyl}}{2 \cdot \dot{m}^2} \tag{8}$$

The ideal gas law is used to determine the density of dry air with (9).

$$\rho = \frac{p}{R_s \cdot T} \tag{9}$$

The pressure, which is needed to calculate the density of dry air, is derived from the difference between the atmospheric pressure p_0 and the pressure drop through the swirl meter, which was kept constant at Δp = 40 mbar. As a result, the swirl number K_S can be calculated from the measured data (10).

$$K_S = \frac{M \cdot (p_0 - \Delta p) \cdot d_{cyl}}{2 \cdot \dot{m}^2 \cdot R_S \cdot T} \tag{10}$$

With the mass flow rate also being recorded at the static flow bench, two flow coefficients can be determined. The flow coefficient $\mu\sigma$ is related to the valve-seat diameter and gives information about the inlet-port quality. The flow coefficient α_k is related to the bore diameter and allows a comparison of different cylinder heads' overall flow performance. The flow coefficients are both defined as a ratio of the measured flow rate $\dot{m}$ to the theoretical flow rate $\dot{m}_{th,Valve/Bore}$ with respect to the applicable geometric reference, (11) and (12).

$$\mu\sigma = \frac{\dot{m}}{\dot{m}_{th,Valve}} \tag{11}$$

$$\alpha_k = \frac{\dot{m}}{\dot{m}_{th,Bore}} \tag{12}$$

The theoretical flow rate $\dot{m}_{th}$, for both valve and bore diameter reference, is calculated using (13) [29].

$$\dot{m}_{th,Valve/Bore} = A_{Valve/Bore} \cdot \rho_{Air,m} \cdot \sqrt{\frac{2 \cdot p_0}{\rho_{Air,m}}} \cdot \sqrt{\frac{\kappa}{(\kappa - 1)}} \cdot \sqrt{\left(1 - \frac{p_1}{p_0}\right)^{\frac{2}{\kappa}} - \left(1 - \frac{p_1}{p_0}\right)^{\frac{\kappa+1}{\kappa}}} \tag{13}$$

Here, A_{Valve} and A_{Bore} are the related geometric references. An isentropic exponent of κ = 1.4 is used for air at 20°C. The density of the moist air around the flow bench $\rho_{Air,m}$ and the static pressure inside the vessel p_1 were derived from recorded data.

With these calculations, the characterization of the respective cylinder heads was enabled. Since increased swirl can result in lower flow rates, both swirl and flow numbers must be examined to evaluate the influence of valve-seat design and inlet-port quality on flow rates and swirl.

C. Experiments on PIV Optical Test Bench

For verification of the static flow bench results and a deeper understanding of the in-cylinder flow pattern, an optically accessible static flow bench was constructed for the visualization of the air flow. Fig. 9 schematically shows the optical test bench at which two-component/two-dimensional (2C/2D) particle image velocimetry (PIV) was utilized to visually evaluate the new valve seat design's impact on the inlet air flow. Information on configuration and used equipment for the PIV can be found in Table 2.

For PIV measurements, the optical test bench was connected to the static flow bench to use a blower, differential pressure gauge and a control system to ensure that the operating parameters were equal to those during the static flow bench testing (see III.B). The distance from the cylinder head's sealing surface to the measurement *x*-*y*-plane was also set to $h_z = D_{bore} \cdot 0.7$.

Both cylinder heads were tested for verification and evaluation of the results from the static flow bench. Hence, PIV measurement results are shown only representatively for valve lifts with high- and low-swirl static test bench results.

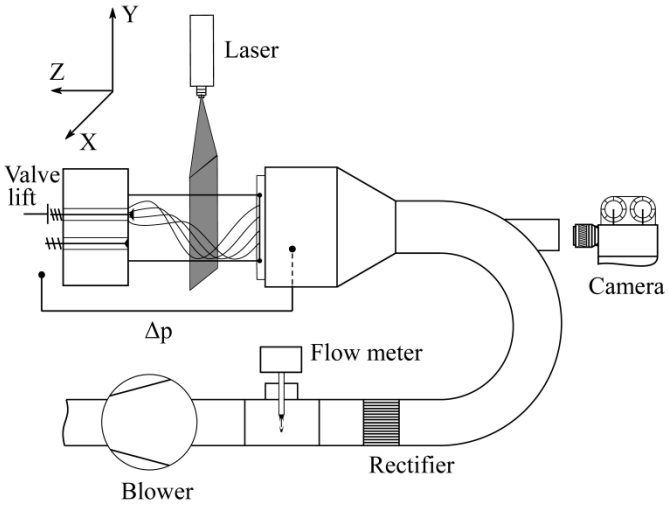

Fig. 9: Schematic setup of the 2D PIV test bench

Images taken with the PIV test bench are transformed to match the established practice of PIV result illustration. The *x*-*y*-plane is the cylinder head sealing surface, the inlet valves are parallel to the *x*-axis and the direction of the view is in the *z*-axis toward the combustion chamber and in the direction of the main air flow. The results include a 2C/2D vector plot in *x*- and *y*-coordinates and velocity components *u* in the *x*- and *v* in *y*-direction.

Table 2: Configuration of 2C/2D PIV

	Configuration	Value
Laser	Type	Double-pulsed Nd:YAG
	Wave length	532 nm
	Pulse distance	50-80 µm
Optics	Aperture	f1.8
	Camera set up	2C/2D
Processing	Software	PivVIEW 3.6.4
	Hardware	PCO.edge5.5 sCMOS 16-bit

D. Experiments on the Engine Test Bench

The test-engine setup is schematically shown in Fig. 10. The applied test engine is sewage gas-driven and equipped with an *AVL* indication system that records the cylinder pressure over the crank angle (φ_{ca}). The indication system used for data

acquisition is the compact combustion-measurement system *INDIMICRO*. The software used to process the data was *INDICOM* version *2.7*. A calculation of the heat released by means of the recorded cylinder pressure was conducted. Hence, the overall engine performance was monitored and evaluated for different load conditions. The results were acquired by averaging the data of 200 recorded cycles for each measured load.

The cylinder pressure was measured with a piezoelectric pressure meter, the crank angle was recorded with the *AVL Crank Angle Encoder* (*365* Series). This system delivered crank angle resolution of 0.5° at 720° combustion cycle duration and an interpolated resolution of 0.1°.

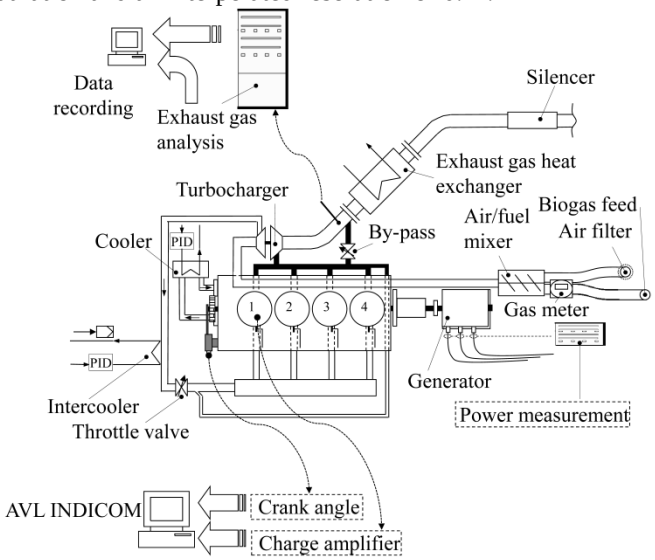

Fig. 10: Schematic setup of the engine test bench

In addition to the crank angle φ_{ca}, the dependent cylinder pressure signal $p(\varphi_{ca})$ volumetric information of the cylinder $V(\varphi_{ca})$ as well as initial temperatures must be available for the calculation of the heat release. With the calculation of the path of the piston $x(\varphi_{ca})$ according to (14) using piston stroke h and connecting rod length l of the motor the cylinder volume $V(\varphi_{ca})$ can be calculated with (15), where ε is the compression ratio and V_H the volume of the cylinder stroke.

$$x(\varphi_{ca}) = \frac{h(1-\cos\varphi_{ca})}{2} + l\left(1 - \sqrt{1-\left(\frac{h}{2l}\cdot sin\varphi_{ca}\right)^2}\right) \quad (14)$$

$$V(\varphi_{ca}) = \frac{V_H}{\varepsilon - 1} + {d_{cyl}}^2 \cdot \frac{\pi}{4} \cdot x(\varphi_{ca}) \quad (15)$$

The heat release dQ_H/dt can be calculated by the thermal energy input supplied by the fuel per time unit, according to (16). The heat release rate is dQ_H, dU is the change of the internal energy of the gas (17) with c_v being the specific heat capacity of the gas at constant volume. The gas temperature change is dT and m is the gas mass burnt inside the cylinder chamber.

$$dQ_H = dU - p \cdot dV \quad (16)$$

$$dU = c_v \cdot dT \cdot m \quad (17)$$

As the resolution of the crank angle is high (at $\varphi_{ca} < 1$), the thermodynamic process can be divided into its adiabatic compression/expansion (18) and isochoric combustion phase (19), thus simplifying calculations and allowing real time calculation of the heat release during engine indication.

$$p2' = p1\left(\frac{V_1}{V_2}\right)^{\kappa} \quad (18)$$

Isochoric combustion is calculated using (19) with the ideal gas law (20), which results in (21)

$$dQ = m \cdot c_v \cdot (T_3 - T_2) \quad (19)$$

$$T = \frac{p \cdot V}{m \cdot R} \quad (20)$$

$$dQ = \frac{c_v}{R} \cdot V_2 \cdot (p_2 - p_{2'}) \quad (21)$$

Combining (18) and (21) gives a convenient way to calculate the heat release, if c_v, the gas constant R and the isentropic exponent $\kappa = 1+R/c_v$ are known (22).

$$dQ_H = \frac{c_v}{R} \cdot V_2 \cdot \left(p2' - p1\left(\frac{V_1}{V_2}\right)^{\kappa}\right) \quad (22)$$

The isochoric heat capacity c_V can be calculated according to (23) using $A_{SI} = 0{,}1$ [30].

$$c_V = 0{,}7 + T \cdot 10^{-3}(0{,}155 + A_{SI}) \quad (23)$$

The electricity produced by the generator and fuel consumption were measured for a defined amount of time once the engine reached a steady state at each set load.

Table 3 shows the results of the engine calibration during the test runs. The set loads were at 100%, 75% and 50% of the engine's nominal power output of 150 kW. The firing point was kept constant at 22° before top dead center (BTDC). The air-to-fuel ratio was controlled to meet the NO_x emission regulation of 500 mg·m^{-3}.

Table 3: Calibration of the cogeneration unit during the test runs

Set load (kW)	150	112	75
Firing point (°)	-22	-22	-22
λ HiGas	1.644	1.58	1.53
λ Baseline	1.643	1.61	1.532
NO_x HiGas (mg·m^{-3})	499	497	498
NO_x Baseline (mg·m^{-3})	494	490	492

The sewage gas that was used was produced onsite at a co-located wastewater purification plant. It consisted of 57.3% methane with a calorific value of 5.75 kWh·m^{-3}. The respective values are presented in Table 4.

Table 4: Methane content and calorific heat value of the applied biogas during the testing

Set load (kW)	150	112	75
Methane HiGas (%)	57.3	57.3	57.3
Methane Baseline (%)	57.7	57.3	57.3
Calorific value HiGas (kWh·m^{-3})	5.74	5.74	5.74
Calorific value Baseline (kWh·m^{-3})	5.76	5.8	5.8

IV. Results and Discussion

A. Static Flow Analysis

The two cylinder heads are examined and compared regarding their flow and swirl coefficients and on-engine performances. Fig. 11 reveals that modifying the geometry near the valve seat has a strong influence on the swirl, particularly at low valve lifts, when the exiting air has a high velocity and the flow passing the sickle shape is forced into a rotational motion. At a valve lift h_v of approximately 8 mm, the swirl flow breaks down, and the tangential motion of the flow pattern changes into a flow with an axial direction to the cylinder axis. With further opening of the valve, decreasing velocity reduces the force with which the air is directed toward the sickle shape so that the swirl drops to the level of the baseline cylinder head. Swirl is then only generated by the arrangement and design of the intake manifolds of the cylinder heads. Since the cylinder heads only differ by the valve-seat design, the swirl reaches the same level once the effect of the sickle shape wears off. The point when the valve-seat design's effect is insignificant can be seen at a valve lift of $h_v > 8$ mm.

The flow coefficient of the non-swirl baseline cylinder head is slightly above the flow coefficient of the sickle-added cylinder head, as swirl leads to increased pressure loss. As both cylinder heads have the same inlet manifold geometry, α_k is used to provide evaluation criteria on the global flow performance of the cylinder heads. The flow coefficient α_k in relation to the valve lift is depicted in Fig. 12. In the case of small valve lifts, the relatively small cross intersection between the valve disc and seat restrict the air flow for both cylinder head variants. This effect is stronger for the sickle-added cylinder head with its sickle shape, due to the redirection of the flow pattern, resulting in higher pressure drops.

To summarize, two effects could be determined that show the potential to contrarily influence combustion. On one hand, the swirl coefficient is expected to increase the combustion rates due to higher turbulence intensity; on the other hand, rising swirl reduces the volumetric efficiency expressed by lower flow coefficients.

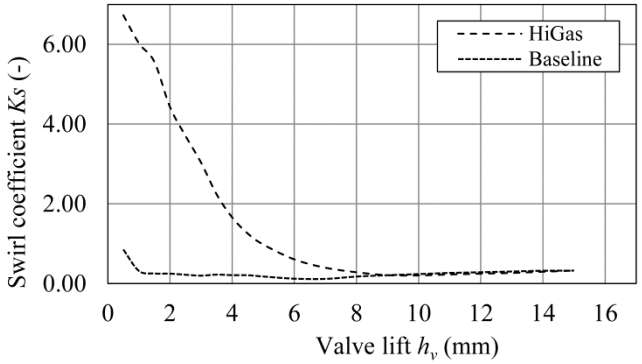

Fig. 11: Comparison of the swirl number *Ks*

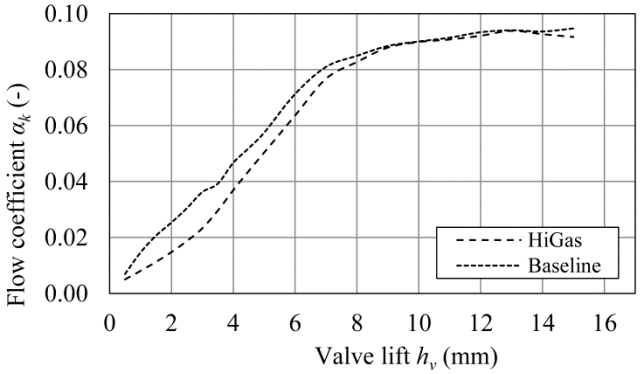

Fig. 12: Comparison of the flow number α_k

The consecutive combustion analysis allows a holistic evaluation of both effects influencing the internal combustion.

B. PIV Optical Flow Analysis

The static flow bench shows significantly higher swirl with the sickle-shaped valve seat design for valve lifts below $h_v = 8$ mm. As the swirl meter is only able to integratively detect movement of air flowing in radial direction, the high swirl inlet flow is expected to have one major rotational flow pattern. Results from the optical test bench using the 2D PIV analysis method show that at an exemplary valve lift of $h_v = 2$ mm which represents generally small valve lifts, the air flowing through the sickle-featured cylinder head has a rotational flow pattern, whereas the flow pattern developed by the baseline cylinder head shows a chaotic multidirectional turbulence field, Fig. 13. As there is no constraint to the flow at small valve lifts by the valve disc, the high air velocity cannot be used for increasing the rotational flow. Turbulence seems high, but maximum measured flow velocity is lower compared to the new cylinder head as air flowing through the valve is distributed to a wider cross-sectional area resulting in a low rotation and therefore small measurable velocities.

As static bench results show a low swirl level for both cylinder heads from $h_v > 8$ mm, a valve lift of 10 mm is shown in Fig. 14, representing valve lifts in which valve seat design effects are expected to have worn off.

A multidirectional flow pattern comparable to the baseline cylinder head, which is illustrated in Fig. 13, can now be seen for both cylinder heads. The flow patterns show similarities around the inlet valve. Furthermore, large areas of very low velocities indicate an axial direction of flow (*z*-axis direction) for both cylinder heads as a wide valve opening results in less flow resistance created by the valve disc. The air sucked through the cylinder head can now more easily follow its natural axial direction. This axial flowing air is likely to bring high turbulence inside the combustion chamber as well. For the sickle shaped cylinder head the maximum measured flow velocities are still significantly higher at $h_v = 10$ mm as the rotational flow patterns are still maintained partially but disrupted by counter-flowing air.

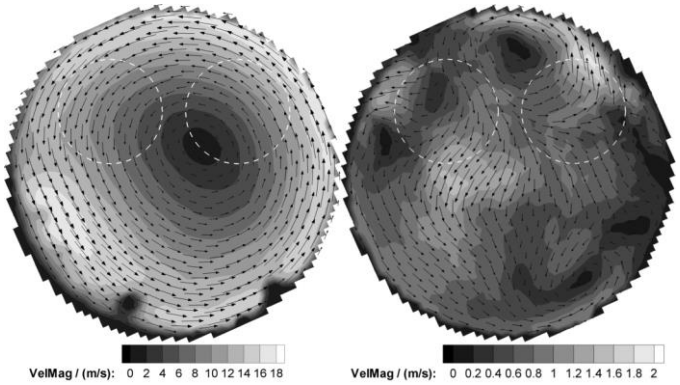

Fig. 13: Comparison of the PIV results at $h_v = 2$ mm. Left is the HiGas cylinder head, right is the reference baseline cylinder head

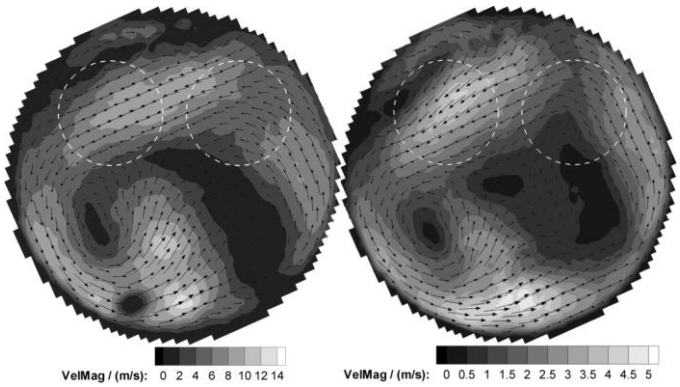

Fig. 14: Comparison of PIV results at $h_v = 10$ mm. Left is the HiGas cylinder head, right is the reference baseline cylinder head

As static flow bench results of the baseline cylinder head show good volumetric efficiency but low swirl performance, it is necessary to run both cylinder heads on an engine test to evaluate how different flow patterns have an impact on combustion performance and motor efficiency.

C. Combustion Analysis

Fig. 15 shows the indicated cylinder pressure in relation to the crank angle (φ_{ca}) at different load conditions. The generated swirl motion proves to overcompensate for the abovementioned reduced volumetric efficiency by showing higher peak pressures. The peak pressure achieved at a full-load condition differs by as much as 20 bars, showing the maximum impact during this study. At partial load, the cylinder pressures are increased as well, but to a lower extent in comparison to full load operation. These results strongly correspond to the thermodynamic background expressed in the introduction of this study.

The combustion process of the test engine is expressed by the normalized heat release rate ($Q_{H,i}$) that shows at which crank angle what ratio of heat has been released (Fig. 16). The curve shows the ignition delay (IGD), which describes the time period between the FP at 22° BTDC and the start of combustion $Q_{H,5\%}$, the center of combustion $Q_{H,50\%}$ and the end of combustion $Q_{H,90\%}$.

At a constant firing point, an earlier crank angle of $Q_{H,i}$ is equal to a faster burning velocity, as it is reached at an earlier timestamp.

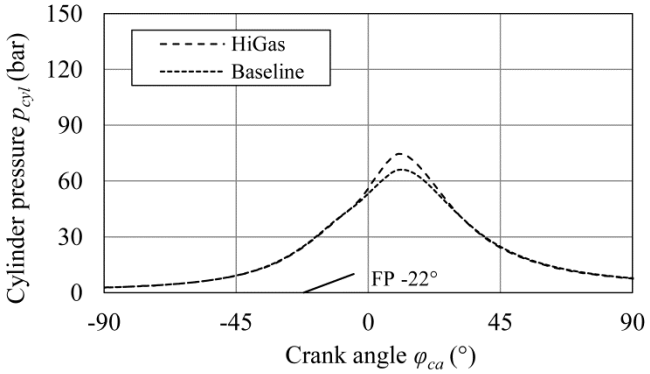

(15a) Cylinder pressure at 75 kW load

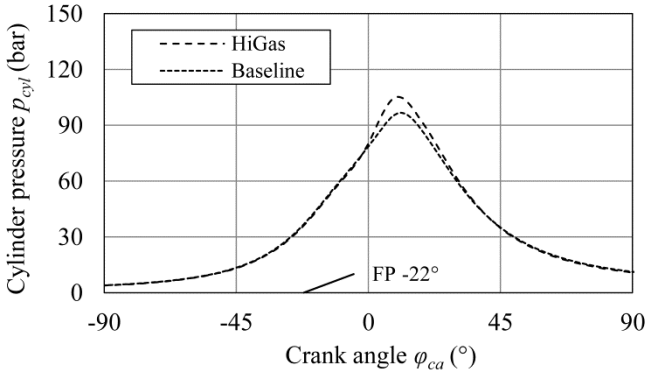

(15b) Cylinder pressure at 112 kW load

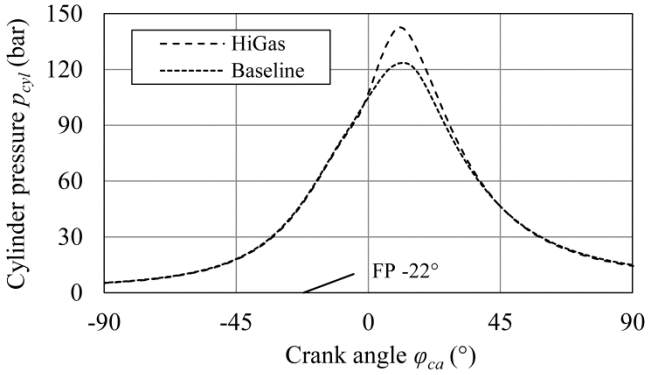

(15c) Cylinder pressure at 150 kW load

Fig. 15: Cylinder pressure over crank angle at different loads (a-c)

To improve comparability, the positions of the $Q_{H,50\%}$ values are listed in Table 5.

Table 5: Measured crank angles for both cylinder heads; describing the internal combustion at different load conditions

Set load (kW)	150	112	75
φ_{ca} $Q_{H,50\%}$ HiGas	8.4°	8.5°	8.35°
φ_{ca} $Q_{H,50\%}$ Baseline	13.05°	11.85°	12.2°
Δ φ_{ca} $Q_{H,50\%}$	-4.65°	-3.35°	-3.85°
φ_{ca} $Q_{H,5\%}$-$Q_{H,90\%}$ HiGas	25.25°	26.4°	24.45°
φ_{ca} $Q_{H,5\%}$-$Q_{H,90\%}$ Baseline	36.95°	35.15°	30.05°
Δ φ_{ca} $Q_{H,5\%}$-$Q_{H,90\%}$	-11.7°	-8.75°	-5.6°
φ_{ca} FP-$Q_{H,5\%}$ HiGas	18.9°	18.55°	18.6°
φ_{ca} FP-$Q_{H,5\%}$ Baseline	19.9°	19.8°	20.45°
Δ φ_{ca} FP-$Q_{H,5\%}$	-1°	-1.25°	-1.85°

The results show a significantly faster combustion at otherwise constant engine parameters. At full load operation (150 kW), the maximum reduction of burning duration ($Q_{H,5\%}$ until $Q_{H,90\%}$) is 11.7° φ_{ca}; at partial load, the reduced combustion duration can be seen as well.

Fig. 17 gives an overview of all combustion benchmarks for both cylinder head variants and all considered load scenarios. It is notable that the burning velocity is nearly equally high for each load condition using the new cylinder head. IGD and $Q_{H,50\%}$ is reached at a similar level independent of the set load. The sickle-shaped valve seats influence the IGD and, furthermore, the position of $Q_{H,50\%}$ and the total burning duration.

The burning duration of the baseline cylinder head strongly depends on the set load, whereas the new sickle-added cylinder head is not affected by fluctuating load conditions.

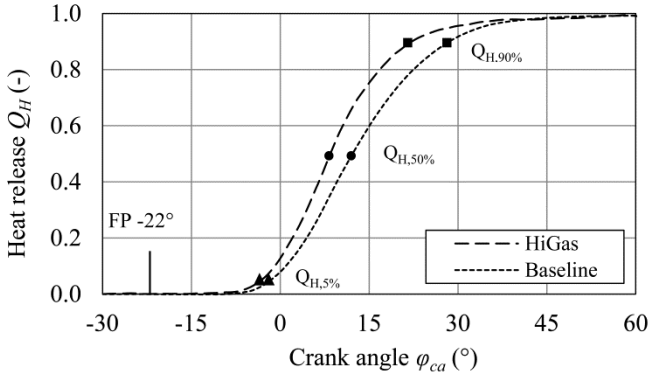

(16a) Heat release rate at 75 kW load

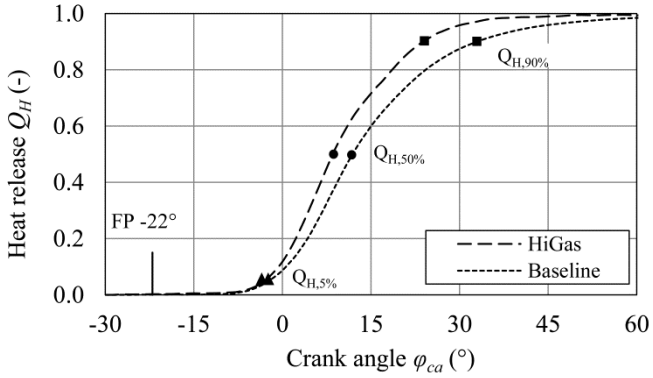

(16b) Heat release rate at 112 kW load

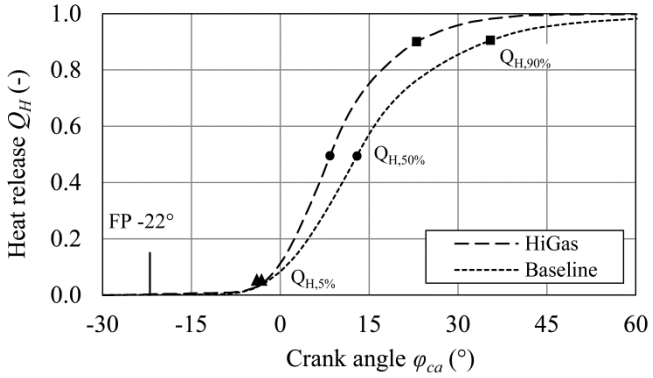

(16c) Heat release rate at 150 kW load

Fig. 16: Combustion rate over crank angle at different loads (a-c). Relevant points of $Q_{H,i}$ drawn into the curves

Considering the electrical efficiency of the cogeneration unit, an increase of up to 1.59% was achieved with the use of the swirl-optimized cylinder head with sickle-shaped valve seats, Table 6. At full and partial loads, the gain in efficiency is significant; at a low partial load operation, only a small increase was measured. With regard to theoretical assumptions, increasing electrical efficiency at low load conditions is expected to be achieved, although it was not measured.

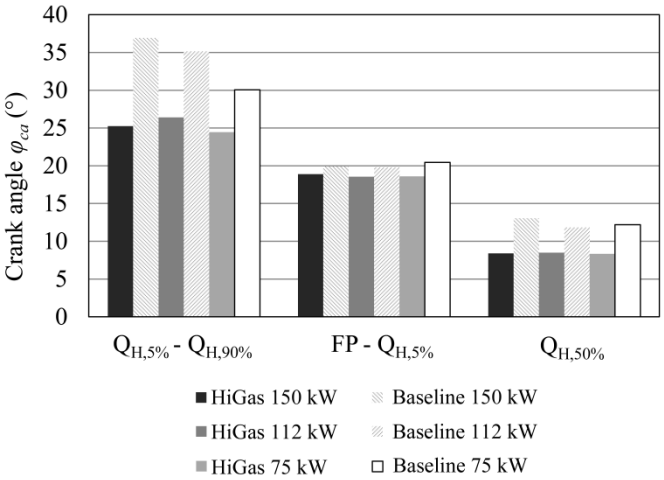

Fig. 17: Comparison of combustion performance fluctuating load conditions

Table 6: Comparison of electric efficiencies

Set load (kW)	150	112	75
η_{el} HiGas (%)	40.28	39.47	37.17
η_{el} Baseline (%)	38.95	37.88	36.13
η_{el} Difference (%)	1.33	1.59	1.04

V. Conclusion

Cylinder heads with two different valve-seat designs were tested on a static flow bench to acquire comparable data describing flow characteristics. Data on the air flow rate and angular momentum generated by the inlet port was used to calculate the flow and swirl coefficients and describe the cylinder heads' static-flow performances. The static flow bench results were compared to results from PIV analysis conducted at an optical test bench for the visualization of flow and velocity patterns. The benchmarked cylinder heads were mounted on a state-of-the-art biogas CHP unit, engine performance was measured and the combustion was analyzed with an indication system.

The sickle-shaped valve seat design has a significant influence on the measured swirl, particularly at small valve lifts when the air flow around the seat has a high velocity. Increased swirl reduces the volumetric efficiency, but the turbulence pattern has the potential to overcompensate for this disadvantage. PIV-results strongly correspond to those findings. At high valve lifts, the air flowing through the cylinder head shows low flow velocities in a radial direction, resulting in low swirl numbers.

The strongly positive influence of the generated swirl on combustion characteristics was shown in all operation conditions. Through all loads, maximum cylinder pressure and

correlating combustion rates were higher with the new valve-seat design. Additionally, the overall combustion velocity did not seem to be affected by the load at which the engine was run. This observation means that the new sickle-shape design is likely to improve burning velocities for all stationary-operated gas engines of similar size. Further research will include a detailed consideration of partial load operation, particularly at 50% of the nominal power output. These already-planned experimental investigations are expected to show the degree of influence of the swirl motion on full- and partial-load operation.

In the course of this study, it was proven that a goal-orientated optimization of the charge motion has the potential to improve internal combustion and, hence, thermal efficiency.

REFERENCES

[1] Lucas Konstantinoff, Dominik Mairegger, Christoph Pfeifer, Uwe Trattnig, Thomas Dornauer, Lukas Möltner (2017): *Turbulent Combustion in Piston Engines driven by Sewage Gas for the Cogeneration of Heat and Power*. In: WSEAS TRANSACTIONS on HEAT and MASS TRANSFER Volume 12, 2017 (E-ISSN: 2224-3461).

[2] T. Shudo, T. Nagano and M. Kobayashi (2003): *Combustion Characteristics of Waste Pyrolysis Gases in an Internal Combustion Engine*. In: International Journal of Automotive Technology (4), P. 1–8.

[3] Kim, Yungjin; Kawahara, Nobuyuki; Tomita, Eiji; Oshibe, Hiroshi; Nishikawa, Koichi (2015): *Effect of Bio-Gas Contents on SI Combustion for a Co-Generation Engine*. In: JSAE/SAE 2015 International Powertrains, Fuels & Lubricants Meeting, SEP. 01, 2015: SAE International400 Commonwealth Drive, Warrendale, PA, United States (SAE Technical Paper Series).

[4] J. Yao-hua, et al. (2009): *Research of Biogas as Fuel for Internal Combustion Engine*. In: 2009 Asia-Pacific Power and Energy Engineering Conference, P. 1–4.

[5] Tewari, P., Subrahmanyam, J., and Babu, M. (2001): *Experimental Investigations on the Performance Characteristics of a Producer Gas Fuelled Spark Ignition Engine*. In: SAE Int. J. Engines. DOI: 10.4271/2001-01-1189.

[6] Wheeler, Jennifer; Stein, Joshua; Hunter, Gary (2014): *Effects of Charge Motion, Compression Ratio, and Dilution on a Medium Duty Natural Gas Single Cylinder Research Engine*. In: SAE Int. J. Engines 7 (4), P. 1650–1664. DOI: 10.4271/2014-01-2363.

[7] Abidin, Zainal; Hoag, Kevin; Mckee, Douglas; Badain, Nicholas (2016): *Port Design for Charge Motion Improvement within the Cylinder*. In: SAE 2016 World Congress and Exhibition, APR. 12, 2016: SAE International400 Commonwealth Drive, Warrendale, PA, United States (SAE Technical Paper Series).

[8] Ogink, Roy; Babajimopoulos, Aristotelis (2016): *Investigating the Limits of Charge Motion and Combustion Duration in a High-Tumble Spark-Ignited Direct-Injection Engine*. In: SAE Int. J. Engines 9 (4). DOI: 10.4271/2016-01-2245.

[9] Porpatham, E.; Ramesh, A.; Nagalingam, B. (2013): *Effect of swirl on the performance and combustion of a biogas fuelled spark ignition engine*. In: Energy Conversion and Management 76, P. 463–471. DOI: 10.1016/j.enconman.2013.07.071.

[10] König, G.; Maly, R. R.; Bradley, D.; Lau, A. K. C.; Sheppard, C. G. W. (1990): *Role of Exothermic Centres on Knock Initiation and Knock Damage*. In: International Fuels & Lubricants Meeting & Exposition, OCT. 22, 1990: SAE International400 Commonwealth Drive, Warrendale, PA, United States (SAE Technical Paper Series).

[11] Wildman, Craig; Cheng, Wai K. (2010): *The Effects of Charge Motion and Laminar Flame Speed on Late Robust Combustion in a Spark-Ignition Engine*. In: SAE Int. J. Engines 3 (1), P. 202–213. DOI: 10.4271/2010-01-0350.

[12] Laget, Olivier; Zaccardi, Jean-Marc; Gautrot, Xavier; Mansion, Thomas; Cotte, Emmanuel (2010): *Establishing New Correlations Between In-Cylinder Charge Motion and Combustion Process in Gasoline Engines Through a Numerical DOE*. In: SAE Int. J. Engines 3 (1), P. 183–201. DOI: 10.4271/2010-01-0349.

[13] Mallard, E., and H. L. Le Chatelier. (1883): *Thermal model for flame propagation.* In: Annales des Mines (Vol. 4. No. 18.), P. 379–568.

[14] Liñán, Amable; Williams, Forman A. (1993): *Fundamental aspects of combustion*. New York: Oxford University Press (Oxford engineering science series, 34). ISBN: 978-0195076264.

[15] Glassman, Irvin; Yetter, Richard A.; Glumac, Nick G. (op. 2015): *Combustion*. 5th ed. Amsterdam [etc.]: Elsevier; Academic Press. ISBN: 978-0124079137.

[16] Lee, Kihyung; Bae, Choongsik; Kang, Kernyong (2007): *The effects of tumble and swirl flows on flame propagation in a four-valve S.I. engine*. In: Applied Thermal Engineering 27 (11-12), P. 2122–2130. DOI: 10.1016/j.applthermaleng.2006.11.011.

[17] Damköhler, Gerhard (1940): *Der Einfluss der Turbulenz auf die Flammengeschwindigkeit in Gasgemischen*. In: Zeitschrift für Elektrochemie und angewandte physikalische Chemie, P. 5–9021. DOI: 10.1002/bbpc.19400461102.

[18] Heywood, John (1988): *Internal Combustion Engine Fundamentals*. 1. Aufl.: McGraw-Hill Science/Engineering/Math. ISBN: 0-07-028637-X.

[19] Joos, Franz (2006): *Technische Verbrennung.* Verbrennungstechnik, Verbrennungsmodellierung, Emissionen. Berlin, Heidelberg: Springer-Verlag Berlin Heidelberg. ISBN: 978-3-540-34334-9.

[20] Benson, G.; Fletcher, E. A.; Murphy, T. E.; Scherrer, H. C. (1983): *Knock (Detonation) Control by Engine Combustion Chamber Shape*. In: SAE International Congress and Exposition, FEB. 28, 1983: SAE International400 Commonwealth Drive, Warrendale, PA, United States (SAE Technical Paper Series).

[21] McKenzie, Jacob; Cheng, Wai K. (2016): *The Anatomy of Knock*. In: SAE 2016 World Congress and Exhibition, APR. 12, 2016: SAE International400 Commonwealth Drive, Warrendale, PA, United States (SAE Technical Paper Series).

[22] Piock, Walter F.; Befrui, Bizhan; Berndorfer, Axel; Hoffmann, Guy (2015): *Fuel Pressure and Charge Motion Effects on GDi Engine Particulate Emissions*. In: SAE Int. J. Engines 8 (2), P. 464–473. DOI: 10.4271/2015-01-0746.

[23] Pischinger, Rudolf; Klell, Manfred; Sams, Theodor (2009): *Thermodynamik der Verbrennungskraftmaschine*. 3. Aufl. Wien, New York, NY: Springer (Der Fahrzeugantrieb). ISBN: 978-3211-99276-0.

[24] Zhang, Dehong; Hill, Philip G. (1996): *Effect of swirl on combustion in a short cylindrical chamber*. In: Combustion and Flame 106 (3), P. 318–332. DOI: 10.1016/0010-2180(95)00256-1.

[25] Masahiko Fujimoto, Kohei Iwai, Motoshi Kataoka, Michihiko Tabata (2002): *Effect of combustion chamber shape on tumble flow, squish-generated flow and burn rate*. In: Society of Automotive Engineers of Japan, Inc.

[26] Tippelmann, Götz (1977): *A New Method of Investigation of Swirl Ports*. In: SAE Technical Paper Series. DOI: 10.4271/770404.

[27] Corberán, José M.; Pérez, Ricardo (1998): *An Alternative Technique for Swirl Measurement*. In: International Congress & Exposition, FEB. 23, 1998: SAE International400 Commonwealth Drive, Warrendale, PA, United States (SAE Technical Paper Series).

[28] Li, Yufeng (2014): *A New Estimation of Swirl Ratio from Steady Flow Rig Testing*. In: SAE 2014 International Powertrain, Fuels & Lubricants Meeting, OCT. 20, 2014: SAE International400 Commonwealth Drive, Warrendale, PA, United States (SAE Technical Paper Series).

[29] Paulweber, Michael; Lebert, Klaus: *Mess- und Prüfstandstechnik.* Antriebsstrangentwicklung - Hybridisierung - Elektrifizierung. ISBN: 978-3-658-04452-7.

[30] Kuratle, Rolf (1995): *Motorenmesstechnik*. Würzburg: Vogel. ISBN: 3-8023-1553-7.